Energy Storage Materials 77 (2025) 104231

Contents lists available at ScienceDirect

Energy Storage Materials

journal homepage: www.elsevier.com/locate/ensm

Plasma-enhanced vacancy engineering for sustainable high-performance recycled silicon in lithium-ion batteries

Dingyi Zhang [a,1], Hong Gao [a,1,*], Jiayi Li [a], Yiwen Sun [a], Zeshen Deng [b], Xinyao Yuan [a], Congcong Li [a], Tianxiao Chen [a], Xingwang Peng [a], Chao Wang [a], Yi Xu [a], Lichun Yang [b,*], Xin Guo [c], Yufei Zhao [d], Peng Huang [e,*], Yong Wang [a], Guoxiu Wang [d], Hao Liu [d,*]

[a] Joint International Laboratory on Environmental and Energy Frontier Materials, School of Environmental and Chemical Engineering, Shanghai University, Shanghai 200444, China
[b] School of Materials Science and Engineering, and Guangdong Provincial Key Laboratory of Advanced Energy Storage Materials, South China University of Technology, Guangzhou 510640, China
[c] Faculty of Materials Science and Energy Engineering, Shenzhen University of Advanced Technology, Shenzhen 518055, Guangdong, China
[d] Centre for Clean Energy Technology, University of Technology Sydney, Broadway, Sydney, NSW 2007, Australia
[e] School of Chemistry and Materials Science, Jiangsu Normal University, Xuzhou, Jiangsu 221116, China

ARTICLE INFO

Keywords:
Lithium-ion batteries
Silicon microparticles
Vacancy engineering
Bismuth modification
Recycled photovoltaic silicon

ABSTRACT

Silicon, renowned for its exceptional theoretical capacity, is a promising lithium-ion battery (LIB) anode material, yet its practical application is hindered by severe lithiation-induced volume expansion, structural instability, and high production costs. This study introduces a sustainable strategy to address these challenges by repurposing recycled photovoltaic (PV) silicon through a plasma-assisted vacancy engineering approach. By combining dielectric barrier discharge plasma-assisted milling with bismuth (Bi) modification, controlled vacancy defects are introduced into silicon microparticles, enhancing ion transport and mitigating internal stress. Bi further stabilizes the anode by absorbing mechanical stress and facilitating lithium-ion accommodation at vacancy sites. The resulting plasma induced silicon/carbon/bismuth composite demonstrates outstanding cycling stability and high-rate performance, retaining 1442 mA h g^{-1} after 300 cycles at 0.5 A g^{-1} and 525 mA h g^{-1} after 1000 cycles at 7 A g^{-1}. This scalable and eco-friendly method not only overcomes the inherent limitations of silicon anodes but also transforms PV waste into high-performance LIB materials, advancing sustainable energy storage technologies.

1. Introduction

Although lithium-ion batteries (LIBs) occupy a predominant position in the domain of energy storage, their development is hindered by the limited capacity of conventional anode materials [1–3]. Silicon (Si), with an exceptional theoretical capacity of up to 4200 mA h g^{-1} (depending on the lithiation phase) and a suitable lithiation voltage plateau ranging from 0.2 to 0.5 V vs. Li^+/Li, emerges as a promising candidate material for the next-generation anodes [4–9]. However, producing battery-grade silicon through traditional refining and processing methods is both energy-intensive and costly, highlighting the urgent need for sustainable and efficient alternatives [10–16]. Meanwhile, the rapid expansion of photovoltaic (PV) module deployment is projected to generate approximately 78 million tons of waste solar panels globally by 2050, posing significant environmental challenges [17,18]. Despite making up 20–25 % of a PV module's weight, silicon is frequently excluded from standard recycling processes because of the high costs and stringent purity standards needed for reuse in solar applications. However, recycled silicon, despite containing impurities, can be effectively modified to serve as a sustainable anode material for LIBs [19,20]. This approach aligns with circular economy principles, enabling efficient reuse while advancing sustainability and environmental responsibility.

Effectively utilizing silicon from PV waste in LIBs requires overcoming its intrinsic limitations, especially the significant volume change during lithiation and delithiation [21,22]. This challenge has driven

* Corresponding authors.
E-mail addresses: hgao1122@shu.edu.cn (H. Gao), mslcyang@scut.edu.cn (L. Yang), huangpeng@jsnu.edu.cn (P. Huang), hao.liu@uts.edu.au (H. Liu).
[1] These authors contributed equally to this work.

https://doi.org/10.1016/j.ensm.2025.104231
Received 23 January 2025; Received in revised form 19 March 2025; Accepted 3 April 2025
Available online 4 April 2025

extensive research into structural and compositional modifications to enhance electrochemical performance of silicon anodes. Designing silicon nanostructures, such as nanowires, thin films and yolk-shell porous structures, exhibit superior adaptability to volume changes due to their high surface area and nanoscale dimensions [23–27]. However, although effective for silicon nanoparticles (SiNPs), these strategies face scalability challenges that limit their industrial applicability [23]. Silicon-carbon (Si-C) composites offer a complementary solution, enhancing electronic conductivity, stabilizing interface, and mitigating silicon's volume expansion during cycling [28–32]. However, when applied to silicon microparticles (SiMPs)-the preferred choice for industrial LIBs due to their lower cost, higher packing density, and scalability [33–35] -conventional methods provide only limited performance improvements, underscoring the need for innovative solutions tailored to SiMPs [36–38]. Vacancy engineering has emerged as a transformative approach to overcome the inherent limitations of SiMPs, such as poor surface reactivity and severe volume expansion during lithiation [39–42]. By introducing controlled vacancy defects, this approach creates pathways for efficient ion and electron transport, facilitates rapid charge transfer, and redistributes mechanical stress, effectively mitigating internal stress and enhancing structural stability.

This work leverages dielectric barrier discharge plasma-assisted milling (DBDP), which combines mechanical milling with high-energy plasma interactions to induce controlled vacancies and optimize SiMP structures for lithiation-induced stress [43–45]. DBDP's precise surface modification increases active sites on SiMPs, enhancing lithium-ion diffusion, reducing interfacial resistance, and significantly improving electrochemical activity and stability [46–48]. While vacancy engineering addresses the structural limitations of SiMPs, adding bismuth (Bi) metal further elevates their electrochemical performance. When compared with other metal additives like lithium, tin, and germanium, lithium, despite its theoretical potential to mitigate lithium loss in the electrolyte, exhibits extremely reactive chemical properties [49]. During experimental operations and the battery manufacturing process, it entails a high safety risk. For instance, it reacts violently upon contact with water or air, presenting formidable challenges to actual production. Tin and germanium metals, on the other hand, encounter the same volume expansion problem as silicon [50,51]. Bismuth, however, can react with lithium ions at a relatively low potential to form a Li-Bi alloy. This process consumes a certain number of lithium ions, reducing the quantity of lithium ions available for deintercalation during the first charging, thereby resulting in a decline in the initial coulombic efficiency. Although metals such as aluminum, titanium, and silver possess certain advantages, such as high conductivity or low reactivity with the electrolyte, they still face significant challenges that limit their practical application. For example, aluminum tends to form a passivation film at the electrode-electrolyte interface, which impedes ion transport. Titanium requires high temperatures and complex processing conditions to form stable compounds with silicon, making it less feasible for large-scale production. Silver, despite its excellent conductivity, is prohibitively expensive for widespread use in battery applications [52–54]. In contrast, bismuth's soft and ductile characteristics enable it to absorb the mechanical stress of expansion and contraction during lithiation/delithiation. This effectively prevents pulverization and enhances the overall integrity of the Si anode [55,56].. Additionally, we detect that bismuth can occupy vacancy sites created through vacancy engineering, enhancing the structural stability of the silicon matrix. Furthermore, the uniform distribution of bismuth within the silicon matrix reduces interfacial resistance, ensuring efficient charge/discharge cycles and promoting the long-term performance of the electrode material [57,58]. Together, vacancy engineering and Bi modification synergistically enable high-performance, durable silicon-based anodes. The resulting plasma induced silicon/carbon/bismuth (P-Si/C/Bi) anode exhibits remarkable cycling stability.

2. Results and discussion

Harnessing the potential of recycled silicon (R-Si) from discarded solar panels, we employ a dielectric barrier discharge plasma-assisted milling (DBDP) technique to fabricate a P-Si/C/Bi composite, integrating graphite and bismuth to engineer a defect-rich, high-performance structure (Fig. 1a). In Fig. 1a, carbon atoms are omitted from lattice positions to enhance the schematic's clarity and focus on core processes and key components. This omission does not imply the absence of carbon atoms in the lattice. Rather, the schematic is designed to concisely illustrate the main synthesis steps and the roles of critical elements for easier interpretation. The process starts with a multi-step pretreatment using solvothermal swelling and thermal decomposition (SSTD), effectively removing impurities and yielding silicon with a purity of 96.42 % for further processing (Fig. S1). During DBDP milling, plasma treatment introduces vacancies and dislocations [59,60], optimizing the microstructure at the atomic level while simultaneously functionalizing the material's surface. This non-thermal plasma process induces grain boundary shifts, increasing surface area and creating active sites that enhance electrochemical performance. Graphite boosts electrical conductivity and buffers silicon's volume expansion during cycling, while bismuth absorbs mechanical stress, preventing pulverization and ensuring anode stability.

As shown in Fig. 1b and Fig. S2, scanning electron microscope (SEM) and atomic force microscopy (AFM) images of the P-Si/C/Bi composite reveal a bulk morphology with an average particle size of approximately 1 μm. DBDP treatment results in a more uniform particle size distribution compared to conventional ball milling. For comparison, materials synthesized via standard ball milling (Si/C) and plasma-assisted milling (P-Si/C) are also analyzed. SEM and AFM images (Fig. S3 and Fig. S4) reveal larger average particle sizes of approximately 1.5 μm and 2.0 μm for P-Si/C and Si/C, respectively. Additionally, SEM images of R-Si, plasma-milled recycled silicon (P-R-Si), and commercial silicon micron particles (SiMPs) (Fig. S5) indicate average particle sizes of approximately 0.8, 0.5, and 1.0 μm, respectively. The improved particle size uniformity observed in the P-Si/C/Bi composite enhances its reactivity and surface area, critical factors underpinning its superior electrochemical performance in LIB applications. The contents of Si and Bi in the composite anode were accurately determined by Inductively Coupled Plasma Mass Spectrometry (ICP-MS). As shown in Table S1, the Si content is 49.08 wt %, while the Bi content is 19.04 wt %. Based on these values, the carbon content is estimated to be around 30 wt %. The crystallinity and phase composition of the P-Si/C/Bi composite are assessed using X-ray diffraction (XRD). The characteristic peaks of silicon and silicon carbide are shown in the XRD patterns of P-Si/C/Bi and P-Si/C, indicating the successful formation of Si-C bonds within these composites. Simultaneously, a minor amount of SiO_2 is also detected, reflecting its inevitable formation during processing (Fig. 1c). In contrast, the Si/C composite shows only the typical silicon peaks, suggesting that plasma-assisted milling significantly enhances silicon-carbon interaction. Furthermore, the XRD patterns of R-Si, P-R-Si, and SiMPs match the standard crystalline silicon pattern (PDF#27–1402), indicating that the silicon crystal structure remains intact after both conventional and plasma-assisted ball milling (Fig. S6). This suggests that DBDP treatment preserves silicon's structural integrity. Complementary Fourier-transform infrared (FTIR) spectroscopy, shown in Fig. 1d, reveals a distinct Si-C vibration peak near 800 cm^{-1} in P-Si/C/Bi and P-Si/C, which is absent in Si/C. This corroborates the formation of Si-C covalent bonds in the plasma-milled composites, further validating the XRD findings. X-ray photoelectron spectroscopy (XPS) analysis, as shown in Fig. 1e-f, provides additional evidence of the Si-C interaction. The full XPS spectrum of P-Si/C/Bi confirms the presence of Si, Bi, C and O elements (Fig. S8). In the Si 2p spectra (Fig. 1e), peaks at 99.77, 101.50, and 103.56 eV correspond to various silicon valence states. Notably, the double peaks at 101.50 and 102.27 eV in P-Si/C/Bi and P-Si/C, absent in Si/C [61–64], indicate the formation of C-Si-C covalent

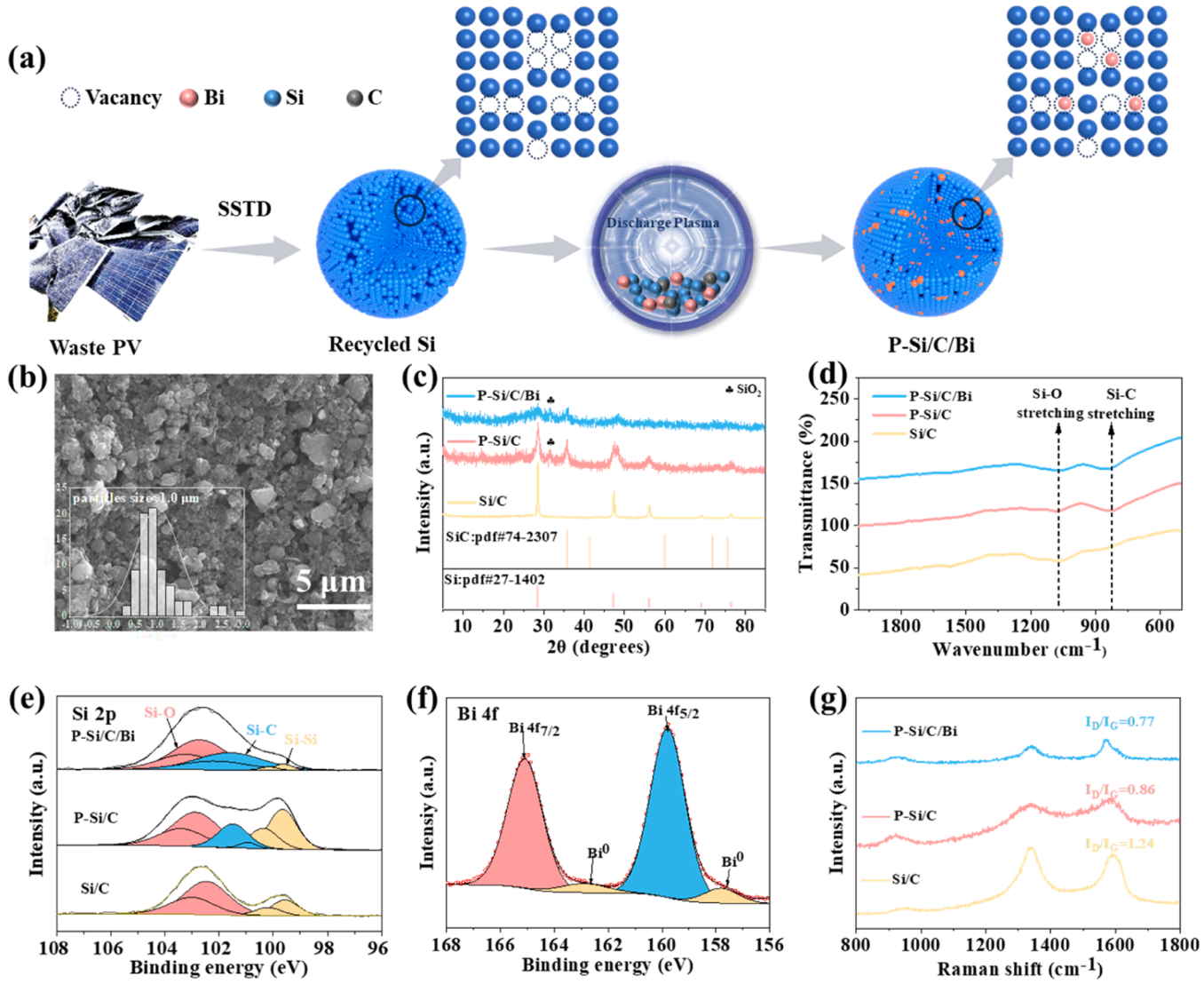

Fig. 1. (a) Fabrication process and conceptual design of P-Si/C/Bi composite. (b) Particle size distribution graph and SEM image of P-Si/C/Bi composite. (c) XRD patterns and (d) FTIR spectra for P-Si/C/Bi, P-Si/C and Si/C. (e) XPS spectra of Si 2p for P-Si/C/Bi, P-Si/C and Si/C. (f) XPS spectrum of Bi 4f for P-Si/C/Bi. (g) Raman spectra of P-Si/C/Bi, P-Si/C and Si/C.

bonds, likely induced by the free radicals, ions, and electrons during DBDP. These robust bonds not only mitigate the volume change of silicon during the cycle, but also enhance structural stability. The incorporation of bismuth also influences the chemical structure, as evidenced by the XPS Bi 4f peaks (Fig. 1f). Peaks at 164.6 and 158.7 eV correspond to Bi $4f_{5/2}$ and Bi $4f_{7/2}$, while peaks at 162.4 and 157.1 eV are attributed to BiO [65], indicating the coexistence of Bi^{3+} in Bi_2O_3 and BiO. Raman spectroscopy (Fig. 1 g) further elucidates the carbon phase's structural order. The I_D/I_G ratio, representing the carbon's disorder degree, is significantly lower in P-Si/C/Bi (0.77) and P-Si/C (0.86) compared to Si/C (1.24), indicating enhanced graphitization and ordered carbon structures in the plasma-milled composites. This improved graphitization supports superior electrochemical performance of the anode material [61,66].

High-resolution transmission electron microscopy (HRTEM) image of the P-Si/C/Bi composite (Fig. 2a) reveals irregular lattice arrangements influenced by plasma treatment, which are indicative of defect introduction [67]. Defects such as dislocations and vacancies can disrupt the crystal's periodicity, leading to alterations in the spots observed in the FFT pattern. Specifically, dislocations may cause the spots to shift or split, while vacancies can result in changes in spot intensity. As shown in Fig. S9 and Fig. 2b-e, some of the diffraction spots exhibit significant displacement, further confirming the presence of dislocation defects in the material. Unlike R-Si (Fig. S9), fast Fourier transform (FFT) images of selected regions (Fig. 2b-e) show isolated vacancies, rather than extensive clusters, suggesting that plasma milling generates localized defects that enhance reactivity without significantly disrupting crystallinity. Conversely, HRTEM images of the P-Si/C reveal continuous multi-vacancy defects across the lattice (Fig. S10). As shown in the Electron Paramagnetic Resonance (EPR) spectrum of Fig. 2f vacancy defect signals of R-Si, P-Si/C/Bi, and P-Si/C are significantly stronger than that of Si/C, with P-Si/C showing the most pronounced vacancy signal. The weaker signal in Si/C indicates that conventional milling tends to disrupt the vacancy structure, whereas plasma milling facilitates their formation and stabilization. Interestingly, the vacancy signal in P-Si/C/Bi is weaker than in P-Si/C, suggesting thatc bismuth occupies a portion of the vacancies. This observation is corroborated by scanning transmission electron microscopy (STEM) image (Fig. 2 g) and elemental mapping of the P-Si/C/Bi composite (Fig. 2h-k), which demonstrate a more uniform elements distribution compared to P-Si/C (Fig. S10a-e) and Si/C (Fig. S11). The overlay maps clearly demonstrate that bismuth is uniformly dispersed within the silicon-carbon matrix in the P-Si/C/Bi

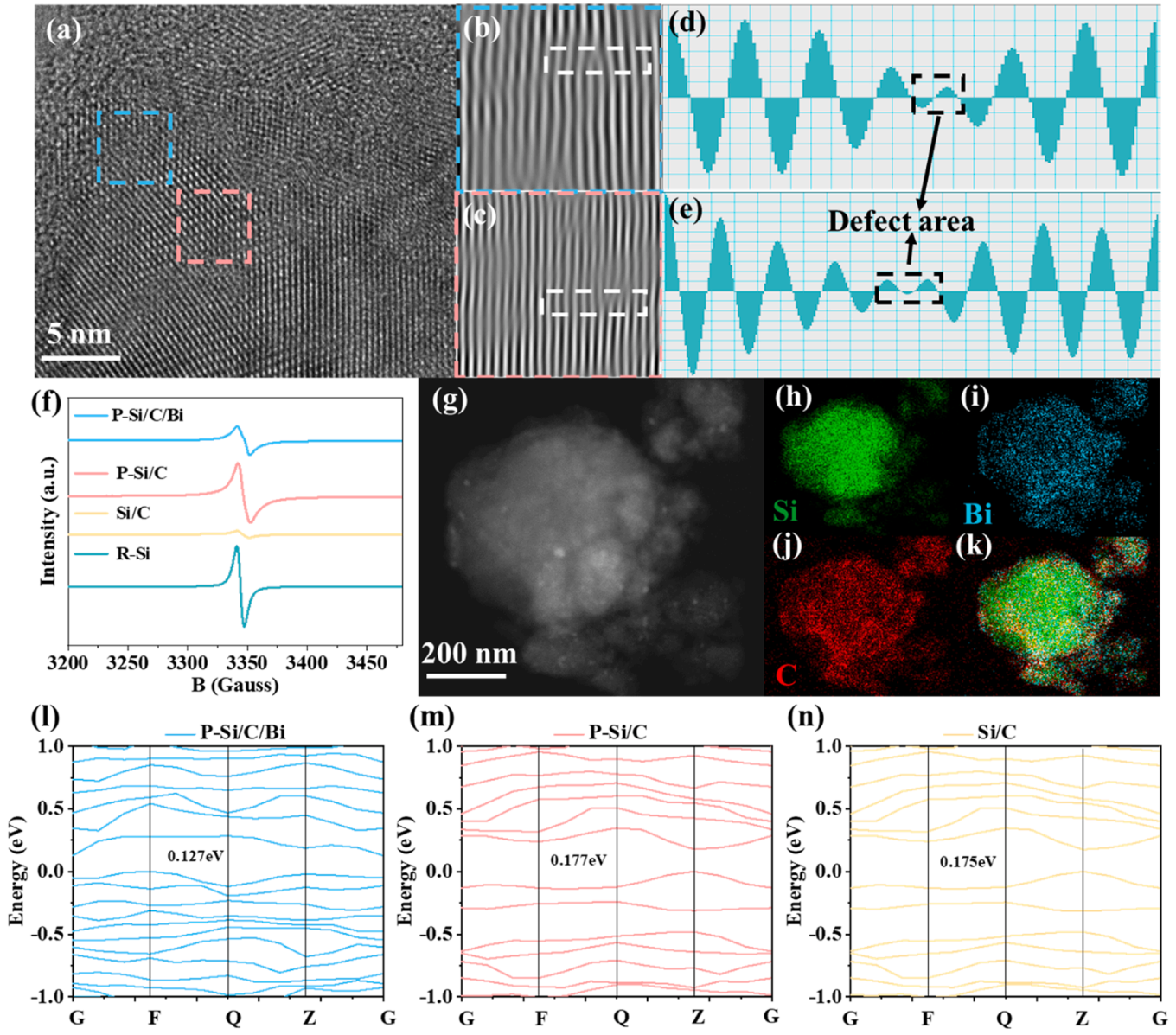

Fig. 2. (a) HRTEM of P-Si/C/Bi, (b, c) corresponding fast Fourier transform (FFT) patterns, and (d, e) phase profile spectra of corresponding regions. (f) EPR spectra of P-Si/C/Bi, P-Si/C, Si/C and R-Si. (g) STEM and (h-k) elemental mapping images of P-Si/C/Bi composite. (l-n) DFT calculations of band structures: (l) P-Si/C/Bi, (m) P-Si/C, and (n) Si/C.

composite, whereas the element distribution in the P-Si/C and Si/C composites is relatively uneven. The incorporation of bismuth plays a dual role: it fills certain vacancies, reducing vacancy signals, while simultaneously enhancing the composite's structural integrity through a uniform distribution. This synergy between defect engineering and uniform bismuth incorporation significantly stabilizes the silicon matrix, promoting improved integration and electrochemical performance. These findings underscore the potential of bismuth-modified silicon composites for advanced battery applications, particularly in enhancing cycling stability and capacity retention.

Fig. 2l-n show the electronic band structures of P-Si/C/Bi, P-Si/C, and Si/C, evaluating the effect of vacancy structures on the electronic properties of materials. The results indicate that P-Si/C, with its multi-vacancy structure, exhibits a band gap of 0.177 eV, slightly higher than the 0.175 eV observed in vacancy-free Si/C. This subtle difference suggests that the vacancy-induced structural changes in P-Si/C may stabilize specific electronic states, marginally altering the band gap. Wide band gaps in both materials hinder carrier transitions, leading to low carrier concentrations and reduced electrical conductivity. In contrast, the incorporation of bismuth in P-Si/C/Bi introduces additional electronic states, narrowing the band gap to 0.127 eV. Moreover, as illustrated in Fig. S12, we evaluated the electrical conductivity of the materials under varying pressures using four-probe measurements. The results indicate that within a specific voltage range, the electrical conductivity of P-Si/C/Bi surpasses that of both P-Si/C and Si/C. Furthermore, the electrical conductivity of P-Si/C is twice that of Si/C. This reduction in band gap facilitates easier electron transitions from the hole carrier concentration to the conduction band, significantly enhancing electrical conductivity and making the material more suitable for high-current and high-voltage environments [48]. The narrower band gap in P-Si/C/Bi also aligns with an increased hole carrier concentration, suggesting a synergistic effect of bismuth on vacancy structures. The interplay between vacancies and bismuth not only tailors the electronic properties but also improves electrochemical stability by promoting charge carrier mobility. These findings underscore the critical role of vacancy engineering and dopant incorporation in optimizing the

electronic and electrochemical characteristics of silicon-based anode materials for advanced LIB applications.

Fig. 3a shows the cyclic voltammetry (CV) curves of the P-Si/C/Bi anode at 0.2 mV s^{-1}. The near perfect overlap of the three curves indicates minimal polarization effects in the P-Si/C/Bi composites. Peaks at 0.77 V and 0.88 V correspond to the alloying/dealloying reactions between Bi and Li, while peaks at 0.15 V and 0.53 V correspond to the alloying/dealloying reactions between Si and Li. In contrast, the CV curves of P-Si/C and Si/C show a typical profile for Si-Li reaction corresponding to the alloying/dealloying reactions of Si and Li, however, the Si/C curves show lower overlap, indicating more pronounced polarization effects. The differential capacity (dQ/dV) curves, shown in Fig. 3b, further corroborate these findings, with oxidation and reduction peaks aligning well with the CV results. The charge and discharge profiles of P-Si/C/Bi for the first, tenth and hundredth cycles are shown in Fig. 3c. In comparison to P-Si/C and Si/C (Fig. S13), the alloying reaction platform of Bi and Li is prominently visible in the P-Si/C/Bi curve, confirming the active participation of Bi in the electrochemical reactions. Regarding the supplementation of BET data for the P-Si/C/Bi electrode (Fig S14), we conducted BET tests on the P-Si/C/Bi, P-Si/C and Si/C electrodes. The results show that the specific surface area of the P-Si/C electrode is 18.6 m^2/g, and that of the Si/C electrode is 60.9 m^2/g. A larger specific surface area may increase the contact area between the electrode and the electrolyte, leading to more side reactions and thus affecting the initial coulombic efficiency. The relatively small specific surface area of the P-Si/C electrode may be one of the reasons why its initial coulombic efficiency is higher than that of the Si/C electrode.

As illustrated in Fig. S15, at a current density of 0.5 A g^{-1}, the specific capacities of both P-R-Si and R-Si decrease significantly over cycles, whereas SiMPs show a relatively smaller reduction. The initial coulombic efficiencies for P-R-Si, R-Si, and SiMPs are recorded as 91.18 %, 89.47 %, and 90.17 %, respectively. These higher initial efficiencies are attributed to the micron-scale particle size of these materials, which enhances the reaction contact area, promoting efficient initial lithiation. However, the large volume expansion of silicon during cycling lead to a pronounced deterioration in their cyclic performance. The initial coulomb efficiencies of P-Si/C/Bi, P-Si/C, and Si/C are 74.32 %, 87.13 % and 84.23 %, respectively. The relatively lower efficiency of P-Si/C/Bi is

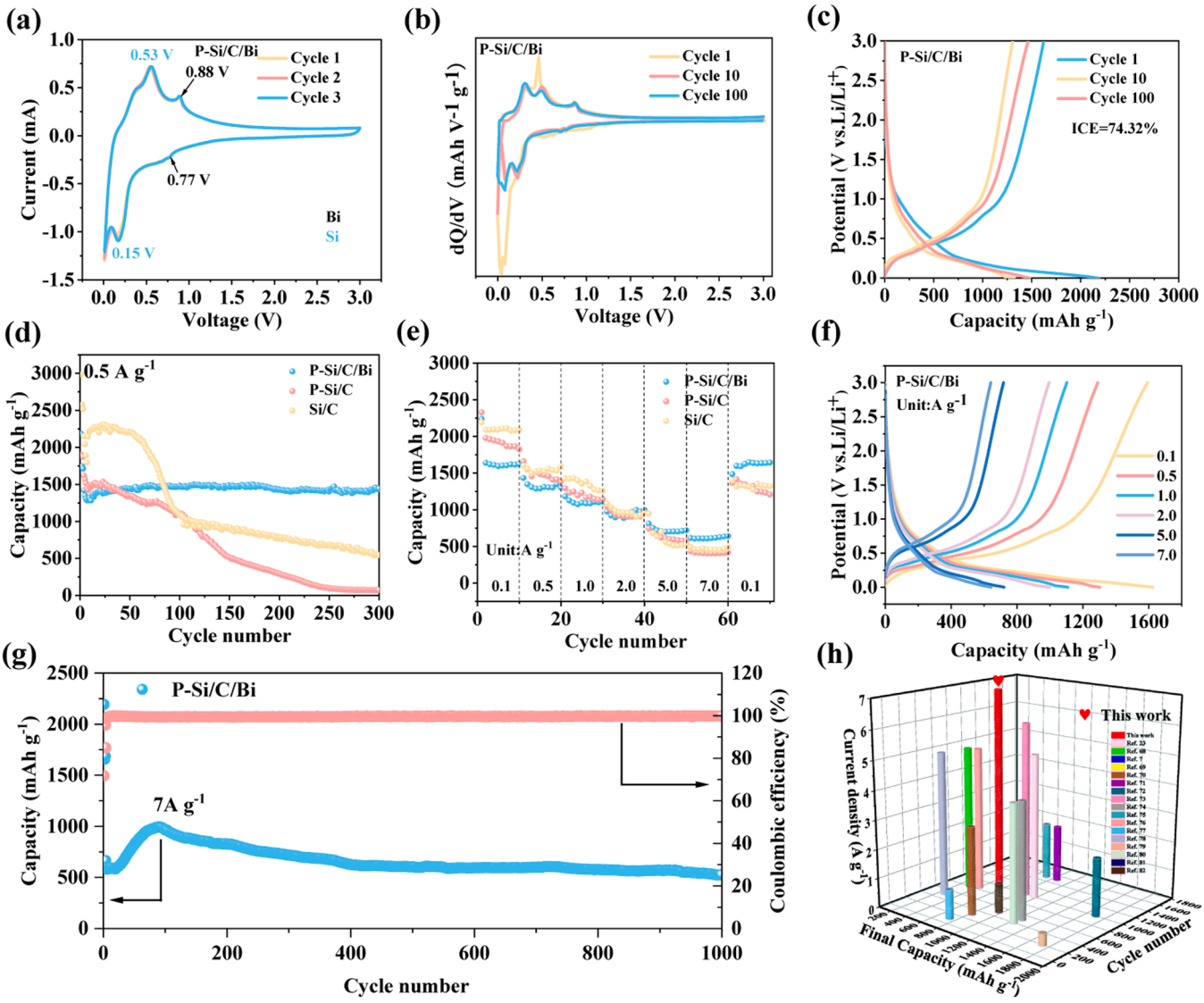

Fig. 3. Electrochemical performance of the P-Si/C/Bi electrode. (a) CV curves at a scan rate of 0.2 mV s^{-1} within the voltage range of 0.01–3.0 V. (b) Differential capacity (dQ/dV) curves of the first, tenth and hundredth cycles at a current density of 0.5 A g^{-1}. (c) Galvanostatic charge/discharge curves at 0.5 A g^{-1}. (d) Cycling performances of P-Si/C/Bi compared with P-Si/C and Si/C electrodes at 0.5 A g^{-1}. (e) Rate performance of the P-Si/C/Bi electrode at different current densities. (f) Charge and discharge profiles at different magnification. (g) Long-term cycling performance of P-Si/C/Bi electrode at 7 A g^{-1}. (h) Comparative analysis of the P-Si/C/Bi anode with other reported anodes in terms of cycle number, current density and final capacity.

attributed to the introduction of bismuth, which participates in additional reactions during the initial cycles. However, the composite demonstrates exceptional cycling stability, attributed to its unique vacancy design and stress-relieving properties. The synergistic effects of bismuth and the engineered vacancies enhance structural integrity, improve long-cycle performance, and mitigate the effects of volume changes during cycling.

Fig. 3d highlights the exceptional cyclic stability of the P-Si/C/Bi electrode compared to P-Si/C and Si/C at a current density of 0.5 A g^{-1}. After 300 cycles, the P-Si/C/Bi electrode retains a capacity of 1442 mA h g^{-1} with a capacity retention rate of nearly 100 %. In contrast, P-Si/C and Si/C show significant performance degradation, retaining only 72.26 and 546.5 mA h g^{-1}, respectively. The corresponding rate performance of the three electrodes is shown in Fig. 3e and 3f, highlighting the rapid charge-discharge capability of P-Si/C/Bi. At a high current density of 7 A g^{-1}, P-Si/C/Bi delivers a specific capacity exceeding 600 mA h g^{-1} and recovers its initial capacity when the current density drops to 0.1 A g^{-1}. This demonstrates the material's excellent electrochemical reversibility and structural integrity. In contrast, P-Si/C and Si/C exhibit lower specific capacities at higher current densities (5 A g^{-1} and 7 A g^{-1}) and fail to fully recover their initial capacities upon reverting to 0.1 A g^{-1}, indicating poorer structural resilience. The long-cycle cycling performance of P-Si/C/Bi at high current density is shown in Fig. 3 g and Fig. S16. At 7 A g^{-1} and 5 A g^{-1}, the P-Si/C/Bi composite retains a capacity of 546.5 mA h g^{-1} and 616.1 mA h g^{-1} after 1000 cycles, with a highly average coulombic efficiency (99.3 %). This result places P-Si/C/Bi among the most durable silicon anodes, as highlighted in Fig. 3h and Table S2 [7,23,68–82]. Additionally, at a current density of 1 A g^{-1}, P-Si/C/Bi achieves a specific capacity of 1019.5 mA h g^{-1} after 500 cycles, outperforming other recycled photovoltaic silicon materials in terms of cyclic stability (Fig. S17 and Table S3). The exceptional electrochemical performance of P-Si/C/Bi is attributed to the synergistic effects of its unique vacancy design and the incorporation of bismuth. The vacancy effectively mitigates the effects of silicon's volume

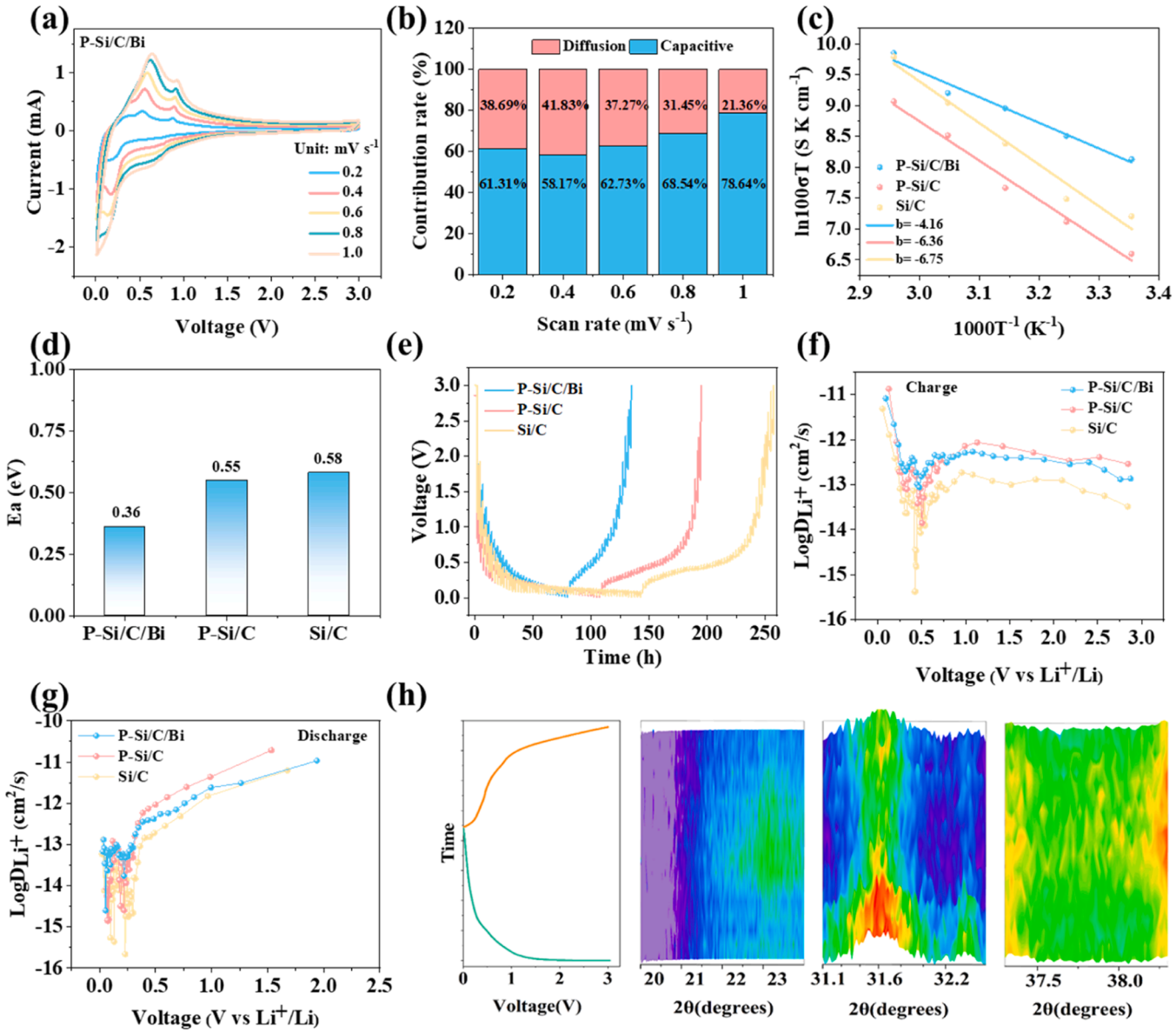

Fig. 4. Electrochemical kinetics and Li^+ diffusion properties of P-Si/C/Bi. (a) CV curves at various scan rates. (b) Contribution ratio of capacitive and diffusion-controlled behaviors at different scan rates. (c) Linear relationships between 1000 T^{-1} (K^{-1}) and ln100σT (S K cm^{-1}) for P-Si/C/Bi, P-Si/C and Si/C. (d) Calculated activation energies, and (e) GITT profiles of P-Si/C/Bi, P-Si/C and Si/C. (f-g) Corresponding Li^+ diffusion coefficients (D_{Li+}) calculated from the GITT profiles. (h) *In-situ* XRD patterns of P-Si/C/Bi electrode at 100 mA g^{-1}.

expansion during cycling, maintaining the structural integrity of the composite. Meanwhile, bismuth not only actively participates in electrochemical reactions but also acts as a buffer to relieve the mechanical stress induced by silicon's expansion and contraction. Together, these features ensure superior stability and capacity retention over extended cycles, making P-Si/C/Bi a highly promising anode material for LIBs.

Fig. 4a-g demonstrates kinetic study of P-Si/C/Bi by using cyclic voltammetry (CV) and the galvanostatic intermittent titration technique (GITT), illustrating the effect of microstructural modifications on the storage behavior of lithium iron. As illustrated in Fig. 4a, the capacity contribution mechanisms of P-Si/C/Bi, P-Si/C, and Si/C electrodes are further investigated through cyclic voltammetry (CV) at scan rates of 0.2, 0.4, 0.6, 0.8, and 1.0 mV s^{-1}. The characteristic oxidation and reduction peaks are consistent across the scan rates, with increasing intensity as the scan rate rises. Notably, the minimal variation in redox peak potential indicates rapid electrode kinetics and high reversibility. The lithium storage mechanisms for these electrodes can be analyzed using the following formula [83]:

$$i = av^b \tag{1}$$

$$i\,(V) = k_1\nu + k_2\nu^{1/2} \tag{2}$$

The charge storage mechanism is identified by the Eq. (1). The value of b can be determined from the relationship between the peak currents (i) and the scan rates (v). A b-value approaching 1 indicates that the capacitive contribution is dominant, while it closer to 0.5 suggests that diffusion-controlled processes is dominant. For the P-Si/C/Bi electrode, the b-values of the redox peaks in the CV curve were fitted (Fig. S18a). The slopes of the fitting curves for the oxidation peak and the reduction peak are 0.859 and 0.856 respectively. Eq. (2) is utilized to quantitatively analyze the contributions of capacitance and diffusion to the current at various scan rates. In this equation, k_1v represents the capacitive-contribution term, and $k_2v^{1/2}$ represents the diffusion-contribution term. We acquire the corresponding values of k_1v and $k_2v^{1/2}$ by fitting the cyclic voltammetry (CV) curves at different scan rates (Fig S18b). Fig. 4b reveals that lithium storage in P-Si/C/Bi is primarily influenced by capacitive contributions, which increase from 61.31 % at 0.2 mV s^{-1} to 78.64 % at 1.0 mV s^{-1}. Electrochemical impedance spectroscopy (EIS) is performed on the three electrodes at varying temperatures (25–65℃) to evaluate ion transport behavior and activation energy. The Nyquist diagram consists of a semicircular region and a slash line, where the semicircular region represents the charge transfer resistance R_{ct} at high frequency, and the slash line represents the low frequency Warburg impedance, indicate that increasing temperature reduces R_{ct}, promoting faster Li^+ diffusion (Fig. S19), Among them, as shown Table S4, at room temperature, the R_{ct} value of P-Si/C/Bi is 79 Ω, which is lower than that of P-Si/C (413.7 Ω) and Si/C (203.7 Ω). The Arrhenius equation is often used to describe the exponential relationship between temperature and chemical reaction rate [84]:

$$k = A \cdot e^{-Ea/(RT)} \tag{3}$$

Where k represents the reaction rate constant, A is the pre-exponential factor indicating the frequency of reactions under ideal conditions, Ea is the activation energy required to overcome the energy barrier, R is the ideal gas constant, in the specific calculation, the Boltzmann constant k_B should be used. T is the absolute temperature in Kelvins. As T increases, the term -Ea/(RT) decreases, causing k to rise. This explains why chemical reactions proceed more rapidly at higher temperatures. By fitting semi-logarithmic function relationship between ion conductivity ln100σT (SK cm^{-1}) and $1000T^{-1}$ (K^{-1}) (Fig. 4c), P-Si/C/Bi, P-Si/C and Si/C slopes are −4.16, −6.36 and −6.75, respectively. P-Si/C/Bi exhibited the lowest activation energy (0.36 eV), compared to 0.55 eV for P-Si/C and 0.58 eV for Si/C (Fig. 4d). underscoring the role of Bi incorporation and plasma ball milling in reducing the energy barrier and enhancing reaction kinetics. The Li^+ diffusion coefficient (D_{Li+}) is further studied by GITT, the corresponding formula is listed as follow [85]

$$D_{Li^+} = \frac{4}{\pi\tau}\left(\frac{m_B V_M}{M_B A}\right)^2 \left(\frac{\Delta E_S}{\Delta E_\tau}\right)^2 \tag{4}$$

Where m_B is defined as the mass of the active material, M_B is the molar mass of the active material, V_M is the molar volume, A is the electrode area, and ΔE_S and ΔE_τ are the voltage change amounts in different stages, respectively. Fig. 4e shows the voltage profiles of P-Si/C/Bi, P-Si/C and Si/C during charging and discharging, and the corresponding D_{Li+} values calculated from the GITT results (Fig. 4f and g) confirming the improved Li^+ diffusion in P-Si/C/Bi compared to P-Si/C and Si/C. Compared with the reported materials, the lithium-ion diffusion coefficient and activation energy of P-Si/C/Bi are superior to those of some reported materials. (Tables S5 and S6). This enhancement is attributed to the reduced activation energy and optimized vacancy structure. *In-situ* XRD measurements are conducted during the charge/discharge process to elucidate the lithium storage mechanisms. Fig. 4h shows the XRD patterns and corresponding voltage profiles, where peaks at 23.7°, 31°, and 37.5° are associated with the formation of Li_xSi, Li_xC, and LiBi [6] respectively. These phase transitions align well with the charge-discharge platforms, demonstrating improved electrochemical reversibility and structural stability of the P-Si/C/Bi electrode during cycling.

Fig. 5a-c and Fig. S20 display the cross-sectional thickness of the electrodes after cycling, elucidating the effects of plasma ball milling and Bi metal incorporation on the volumetric expansion behavior of silicon during cycling. After 10 cycles, the cross-sectional thicknesses for P-Si/C/Bi, P-Si/C, and Si/C electrodes are measured at 32.5 μm, 33 μm, and 42.5 μm, corresponding to expansion ratios (ER) of 18.18 %, 37.5 %, and 41.67 %, respectively. After 100 cycles, the cross-sectional thicknesses increase to 39 μm, 40.5 μm, and 71 μm, with expansion ratios of 41.81 %, 68.75 %, and 136.7 %. The significantly lower ER of P-Si/C/Bi highlights its superior structural stability compared to P-Si/C and Si/C. Electrode surface analysis post-cycling, as depicted in Fig. S21, further underscores this stability. After 10 cycles, substantial cracks were observed on Si/C electrode surfaces, while minimal cracking is evident on P-Si/C and P-Si/C/Bi. Following 100 cycles, the cracks on the Si/C surface had widened significantly, and some cracks appeared on P-Si/C. However, the P-Si/C/Bi surface showed only a few fine cracks, which is crucial for maintaining stable contact between the current collector and the electrode material. The EIS results post-cycling also demonstrated markedly higher impedance levels in Si/C electrodes compared to P-Si/C/Bi and P-Si/C (Fig. S22), further confirming the structural and electrochemical advantages of the P-Si/C/Bi electrode. To evaluate the thermal stability of the P-Si/C/Bi composite anode under high-rate cycling conditions, we conducted Differential Scanning Calorimetry (DSC) and Thermogravimetric Analysis (TGA) tests (Fig. S23). The DSC results indicate that the heat flow curve remains stable during high-rate cycling, with no significant endothermic or exothermic peaks. This suggests the absence of strong chemical reactions or phase transitions, highlighting the material's improved thermal stability. Additionally, TGA analysis shows negligible mass loss within the tested temperature range, further confirming the composite's stability under high-temperature conditions. To verify its practical feasibility, P-Si/C/Bi is paired with nickel-cobalt-manganese oxide (NCM811) to construct a full battery system. As shown in Fig. S24a, the battery retained a high reversible capacity of nearly 400 mA h g^{-1} after 50 cycles at a current density of 100 mA g^{-1}. The voltage-specific capacity curves of the P-Si/C/Bi//NCM811 reveal an average discharge plateau at≈3.6 V within a voltage window of 2.8–4.3 V, demonstrating the promising potential of the P-Si/C/Bi anode for practical application of LIBs (Fig. S24b).

COMSOL Multiphysics simulations (Fig. 5d-i and Fig. S25–26) reveal the mechanism underlying the enhanced mechanical stability of the anode affected by size changes, lithium concentration distribution, and

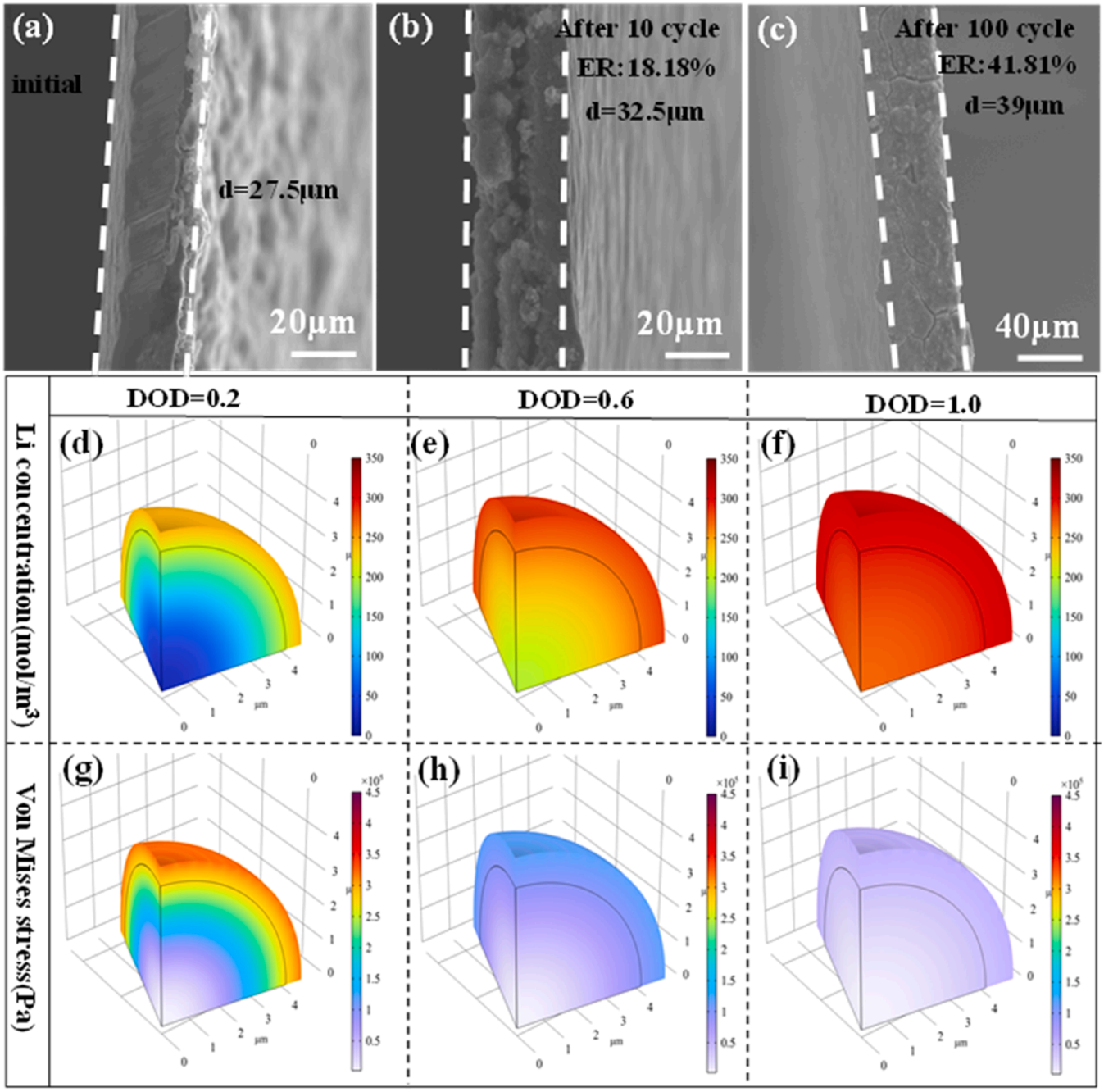

Fig. 5. Structural evolution and stress analysis of the P-Si/C/Bi electrode during cycling. (a-c) SEM cross-section profiles of the P-Si/C/Bi electrodes in its initial state, after 10 cycles, and after 100 cycles, respectively. (d-f) Finite element simulations showing the lithium concentration distribution within the P-Si/C/Bi anode at varying depths of lithiation. (g-i) Corresponding Von Mises stress distribution in the P-Si/C/Bi anode at different depths of lithiation. The diameter of each single particle is 5 μm.

stress states of individual anode particles during lithiation [86,87]. Table S7 provides details on the simulation parameters, including the lithium diffusion coefficient, material composition (mass fraction), and Young's modulus. The input parameter is the external lithium concentration, while the stress originates from strain induced by lithium insertion, with a lithium insertion strain coefficient of 8.85 cm^3/mol. The Young's modulus value corresponds to that of lithium metal. This single-particle simulation serves as a qualitative analysis, where the parameters do not affect the comparative results but only influence the absolute values. During discharge, lithium insertion begins at the particle surface and progresses inward, forming a concentration gradient that induces varying degrees of volume expansion and stress. Fig. 5d-f show the Li concentration distribution in the P-Si/C/Bi anode at different depths of discharge (DODs: 0.2, 0.6, 1.0). The results show that the Li concentration in P-Si/C/Bi particles is more uniform and reaches higher overall levels compared to P-Si/C (Fig. S25) and Si/C (Fig. S26) anodes at the same DOD. The P-Si/C/Bi anode exhibits rapid lithium homogenization, while P-Si/C and Si/C anodes display slower lithium diffusion and pronounced phase boundaries between Li-rich and Li-poor regions. This uneven lithium distribution leads to greater volume strain variations in the Si/C anode, moderate strain in the P-Si/C anode, and highly uniform volume strain P-Si/C/Bi (Fig. 5i). The non-uniform lithiation-induced expansion observed in P-Si/C and Si/C anodes resulted in elevated Von Mises stress levels, increasing the likelihood of

mechanical failure. In contrast, the P-Si/C/Bi anode maintains lower stress levels and uniform volume strain, underscoring its superior structural resilience during cycling. Beyond theoretical simulations, we carried out tensile stress-strain tests on the electrodes. As depicted in the Fig. S27, P-Si/C/Bi exhibits the highest tensile strain (5.43 %), compared to Si/C (5.01 %) and P-Si/C (5.26 %). This indicates that P-Si/C/Bi can undergo significant plastic deformation, dispersing and consuming stress to alleviate stress concentration. This property enhances the mechanical stability and electrochemical performance of the electrode materials, with significant implications for developing high-performance lithium-ion batteries.

3. Conclusions

This study establishes a pioneering framework for advancing silicon-based anodes in lithium-ion batteries by leveraging plasma-assisted vacancy engineering and strategic bismuth integration. Through plasma-assisted ball milling, a defect-rich P-Si/C/Bi composite was synthesized, effectively addressing silicon's intrinsic challenges of severe volume expansion and mechanical instability during cycling. The incorporation of bismuth not only stabilizes the silicon matrix but also mitigates mechanical strain, enabling enhanced capacity retention and prolonged cycle life. The P-Si/C/Bi anodes exhibit exceptional lithium-ion diffusion, superior conductivity, and uniform strain distribution, significantly reducing particle fracture risks. Finite element simulations reveal markedly lower Von Mises stress in P-Si/C/Bi compared to P-Si/C and Si/C, underscoring its outstanding mechanical stability. Achieving discharge capacities of 1442 mA h g^{-1} after 300 cycles at 0.5 A g^{-1} and 546.5 mA h g^{-1} after 1000 cycles at 7.0 A g^{-1}, the anodes demonstrate remarkable durability and electrochemical performance. Beyond technical advancements, this work introduces a sustainable solution to repurpose photovoltaic silicon waste, promoting circular economy principles by transforming discarded materials into high-value anode components. This dual approach of bismuth enhancement and vacancy engineering not only redefines silicon's potential in energy storage but also aligns with global sustainability objectives, setting a new benchmark for green energy innovations.

4. Experimental section

Preparation of materials: The waste solar cells, supplied by SCI Materials Hub without further purification, were cut into micro-modules and loaded in a reactor containing organic solvents. The modules were heated at 190 ℃ for 2 h to remove the surface toughened glass and Ethylene-Vinyl Acetate Copolymer (EVA) layer, then crushed with a mortar to obtain waste silicon powder. To eliminate surface impurities, the silicon powder was treated with phosphoric acid and hydrochloric acid to remove Ag, Al and anti-reflective coating (ARC) layers. The purified silicon powder was transferred into a ball mill tank with a ball-to-powder mass ratio of 80:1. For composite preparation, graphite and bismuth metal were purified powders. Plasma ball milling was employed for P-Si/C/Bi and P-Si/C composites, while Si/C was prepared by conventional planetary ball mill. The milling process was conducted for 12 h at a rotational speed of 600 rpm. Among them, the high-voltage input current of the plasma generator is 1.4 A, the high-voltage input voltage is a pulsed voltage of 23,000 V, and the material of the ball milling jar is stainless steel.

Material Characterization: The fine structural details and morphology of the samples were collected by a ZEISS Gemini-SEM 300 scanning electron microscope (accelerating voltage: 15 kV) and a JEOL-2100F high-resolution transmission electron microscope (HR-TEM, accelerating voltage: 200 kV). Atomic force microscopy (AFM) was used to analyze the topography, particles size, and particles size distribution. X-ray photoelectron spectroscopy (XPS) was conducted using an ESCALAB 250Xi system. X-ray diffraction (XRD, Rigaku D/MAX 2200 V) patterns were achieved with a Rigaku D/MAX 2200 V diffractometer using Cu Ka radiation over a 2θ range of 5°−85° at a scanning rate of 8° min^{-1}. *In-situ* XRD test was carried out using a Swagelok cell equipped with a beryllium window.

Electrochemical Section: The electrochemical performance of the three samples was evaluated using prepared standard CR-2032-coin cells ($H_2O < 10^{-2}$ ppm, $O_2 < 10^{-2}$ ppm) assembled in a glovebox filled with argon gas. The electrodes in the half cell were prepared by mixing the active materials, carboxy-methyl-cellulose sodium and conductive carbon with a mass ratio of 6:2:2. The electrode materials were coated on a copper foil and dried under vacuum at 80 °C for 12 h. The areal mass loadings of the electrode materials on the copper foil were about 1.0–1.3 mg cm^{-2}. Celgard 2400 served as the separator, and pure Li metal was used as the counter electrode. Each coin cell was assembled with 50 μL of electrolyte, consisting of 1 M $LiPF_6$ dissolved in a 1: 1 (v/v) mixture of ethylene carbonate (EC) and diethyl carbonate (DEC), with fluoroethylene carbonate (FEC) as an additive. Cyclic voltammetry (CV) was performed using a CHI 660D workstation at a scan rate of 0.2 mV s^{-1} within a scan range of 0.01–3.0 V vs Li^+/Li. Constant current charge/discharge measurements were conducted at room temperature over the same voltage range using a Neware battery testing system. Electrochemical impedance spectroscopy (EIS) was also performed using the CHI 660D workstation, with a frequency range of 100 kHz to 0.01 Hz. NCM811 powder was mixed with conductive carbon and polyvinylidene fluoride (PVDF) in a 9:0.5:0.5 wt ratio, dispersed in N-methyl-2-pyrrolidone (NMP), and coated onto aluminum foil. The electrodes were vacuum-dried at 120 °C overnight. Full cells were assembled with NCM811 as the cathode and the pre-cycled anode (charged/discharged for five cycles before assembly) in a weight ratio of 1:4. The electrolyte used was the same as in the half-cells (1 M $LiPF_6$ in EC: DEC with FEC).

CRediT authorship contribution statement

Dingyi Zhang: Writing – review & editing, Writing – original draft, Investigation, Formal analysis, Data curation. **Hong Gao:** Writing – review & editing, Writing – original draft, Project administration, Funding acquisition, Formal analysis, Conceptualization. **Jiayi Li:** Writing – review & editing, Investigation, Formal analysis, Data curation. **Yiwen Sun:** Writing – review & editing, Writing – original draft, Software, Methodology, Data curation. **Zeshen Deng:** Writing – review & editing, Methodology, Data curation. **Xinyao Yuan:** Writing – review & editing, Formal analysis, Data curation. **Congcong Li:** Writing – review & editing, Formal analysis, Data curation. **Tianxiao Chen:** Writing – review & editing, Investigation, Formal analysis. **Xingwang Peng:** Writing – review & editing, Data curation. **Chao Wang:** Writing – review & editing, Formal analysis. **Yi Xu:** Writing – review & editing, Software, Resources. **Lichun Yang:** Writing – review & editing, Resources, Project administration, Methodology, Conceptualization. **Xin Guo:** Writing – review & editing, Resources, Methodology. **Yufei Zhao:** Writing – review & editing, Project administration, Formal analysis. **Peng Huang:** Writing – review & editing, Resources, Project administration, Methodology, Formal analysis. **Yong Wang:** Writing – review & editing, Project administration. **Guoxiu Wang:** Writing – review & editing, Project administration, Funding acquisition. **Hao Liu:** Writing – review & editing, Writing – original draft, Supervision, Resources, Project administration, Conceptualization.

Declaration of competing interest

The authors declare the following financial interests/personal relationships which may be considered as potential competing interests:

Hao Liu reports financial support was provided by Australian Research Council. Hong Gao reports financial support was provided by Science and Technology Commission of Shanghai Municipality. If there are other authors, they declare that they have no known competing financial interests or personal relationships that could have appeared to influence the work reported in this paper.

Supplementary materials

Supplementary material associated with this article can be found, in the online version, at doi:10.1016/j.ensm.2025.104231.

Data availability

No data was used for the research described in the article.

References

[1] S. Chu, A. Majumdar, Opportunities and challenges for a sustainable energy future, Nature 488 (2012) 294–303, https://doi.org/10.1038/nature11475.

[2] D. Larcher, J.M. Tarascon, Towards greener and more sustainable batteries for electrical energy storage, Nat. Chem. 7 (2015) 19–29, https://doi.org/10.1038/nchem.2085.

[3] H. Liu, X. Liu, W. Li, X. Guo, Y. Wang, G. Wang, D. Zhao, Porous carbon composites for next generation rechargeable lithium batteries, Adv. Energy Mater. 7 (2017) 1700283, https://doi.org/10.1002/aenm.201700283.

[4] M.T. McDowell, S.W. Lee, W.D. Nix, Y. Cui, 25th anniversary article: understanding the lithiation of silicon and other alloying anodes for lithium-ion batteries, Adv. Mater. 25 (2013) 4966–4985, https://doi.org/10.1002/adma.201301795.

[5] C.K. Chan, H. Peng, G. Liu, K. McIlwrath, X.F. Zhang, R.A. Huggins, Y. Cui, High-performance lithium battery anodes using silicon nanowires, Nat. Nanotechnol. 3 (2008) 31–35, https://doi.org/10.1038/nnano.2007.411.

[6] Z. Zhang, H. Wang, M. Cheng, Y. He, X. Han, L. Luo, P. Su, W. Huang, J. Wang, C. Li, Z. Zhu, Q. Zhang, S. Chen, Confining invasion directions of Li^+ to achieve efficient Si anode material for lithium-ion batteries, Energy Storage Mater 42 (2021) 231–239, https://doi.org/10.1016/j.ensm.2021.07.036.

[7] C. Xu, L. Shen, W. Zhang, Y. Huang, Z. Sun, G. Zhao, Y. Lin, Q. Zhang, Z. Huang, J. Li, Efficient implementation of kilogram-scale, high-capacity and long-life Si-C/TiO_2 anodes, Energy Storage Mater 56 (2023) 319–330, https://doi.org/10.1016/j.ensm.2023.01.025.

[8] N.M. Saidi, M.A.A.M. Abdah, M.N. Mustafa, R. Walvekar, M. Khalid, A. Khosla, Advancements in silicon anodes for enhanced lithium-ion batteries performance: innovations toward next-gen superbatteries, Battery Energy (2025) e20240048, https://doi.org/10.1002/bte2.20240048.

[9] J. Shen, S. Zhang, H. Wang, R. Wang, Y. Hu, Y. Mao, R. Wang, H. Zhang, Y. Du, Y. Fan, Y. Zhou, Z. Guo, B. Wang, Unlocking the potential of silicon anodes in lithium-ion batteries: a claw-inspired binder with synergistic interface bonding, eScience 4 (3) (2024), https://doi.org/10.1016/j.esci.2023.100207.

[10] J. Pan, H. Lu, D. Wu, N. Wang, Q.H. Yang, S. Dou, Revealing the interfacial chemistry of silicon anodes with polysiloxane electrolyte additives, Energy Storage Mater 72 (2024) 103701, https://doi.org/10.1016/j.ensm.2024.103701.

[11] Y. He, L. Jiang, T. Chen, Y. Xu, H. Jia, R. Yi, D. Xue, M. Song, A. Genc, C. Bouchet Marquis, L. Pullan, T. Tessner, J. Yoo, X. Li, J.G. Zhang, S. Zhang, C. Wang, Progressive growth of the solid–electrolyte interphase towards the Si anode interior causes capacity fading, Nat. Nanotechnol. 16 (2021) 1113–1120, https://doi.org/10.1038/s41565-021-00947-8.

[12] G. Zhu, W. Luo, L. Wang, W. Jiang, J. Yang, Silicon: toward eco-friendly reduction techniques for lithium-ion battery applications, J. Mater. Chem. A. 7 (2019) 24715–24737, https://doi.org/10.1039/c9ta08554h.

[13] W.U. Rehman, H.W.R.Z.A. Manj, W. Luo, J. Yang, When silicon materials meet natural sources: opportunitiesand challenges for low-cost lithium storage, Small 17 (2019) 1904508, https://doi.org/10.1002/smll.201904508.

[14] R. Deng, N.L. Chang, Z. Ouyang, C.M. Chong, A techno-economic review of silicon photovoltaic module recycling, Renew. Sust. Eengy Rev. 109 (2019) 532–550, https://doi.org/10.1016/j.rser.2019.04.020.

[15] G. Zhang, H. Gao, D. Zhang, J. Xiao, L. Sun, J. Li, C. Li, Y. Sun, X. Yuan, P. Huang, Y. Xu, X. Guo, Y. Zhao, Y. Wang, G. Wang, H. Liu, Transformative catalytic carbon conversion enabling superior graphitization and nanopore engineering in hard carbon anodes for sodium-ion batteries, Carbon Energy 7 (2025) e713, https://doi.org/10.1002/cey2.713.

[16] J. Xiao, H. Gao, Y. Xiao, S. Wang, C. Gong, Z. Huang, B. Sun, C. Dong, X. Guo, H. Liu, G. Wang, A hydro-stable and phase-transition-free P2-type cathode with superior cycling stability for high-voltage sodium-ion batteries, Chem. Eng. J. 506 (2025) 160010, https://doi.org/10.1016/j.cej.2025.160010.

[17] Y. Liu, Y. Chen, Y. Chen, S. Huang, H. Huang, S. Lin, C. Yang, Utilization of Si/SiO_x/Al_2O_3 materials from recycled solar cells for a high-performance lithium-ion battery anode, Green Chem 24 (2022) 5151–5161, https://doi.org/10.1039/d2gc01770a.

[18] A. Paiano, Photovoltaic waste assessment in Italy, Renew. Sust. Eengy Rev. 41 (2015) 99–112, https://doi.org/10.1016/j.rser.2014.07.208.

[19] Y. Zhang, Z. Zhang, W. Chen, X. Zhang, Z. Guan, Recycling of waste silicon powder from the photovoltaic industry into high performance porous Si@void@carbon anodes for Li-ion battery, Mater. Today Commun. 40 (2024) 109322, https://doi.org/10.1016/j.mtcomm.2024.109322.

[20] W. An, P. He, Z. Che, C. Xiao, E. Guo, C. Pang, X. He, J. Ren, G. Yuan, N. Du, D. Yang, D.L. Peng, Q. Zhang, Scalable synthesis of pore-rich Si/C@C core–Shell-structured microspheres for practical long-life lithium-ion battery anodes, ACS Appl. Mater. Inter. 14 (2022) 10308–10318, https://doi.org/10.1021/acsami.1c22656.

[21] R. He, H. Li, A. Chen, L. Mai, L. Zhou, Mitigating the capacity fading of Si nanoparticles through V_2O_3 and carbon dual coatings, J. Mater. Sci. Technol. 191 (2024) 17–22, https://doi.org/10.1016/j.jmst.2023.12.034.

[22] H. Li, Z. Wang, L. Dang, K. Yu, R. Yang, A. Fu, X. Liu, Y.-G. Guo, H. Li, X.S. Zhao, Si nanoparticles enclosed in hierarchically structured dual-component porous carbon as superior anode for lithium-ion batteries: structure formation and properties investigation, Energy Storage Mater 70 (2024) 103547, https://doi.org/10.1016/j.ensm.2024.103547.

[23] Z. Li, M. Han, P. Yu, J. Lin, J. Yu, Macroporous directed and interconnected carbon architectures endow amorphous silicon nanodots as low-strain and fast-charging anode for lithium-ion batteries, Nano-Micro Lett 16 (2024) 98, https://doi.org/10.1007/s40820-023-01308-x.

[24] H.T. Nguyen, F. Yao, M.R. Zamfir, C. Biswas, K.P. So, Y.H. Lee, S.M. Kim, S.N. Cha, J.M. Kim, D. Pribat, Highly interconnected Si nanowires for improved stability Li-ion battery anodes, Adv. Energy Mater. 1 (2011) 1154–1161, https://doi.org/10.1002/aenm.201100259.

[25] C. Yu, X. Li, T. Ma, J. Rong, R. Zhang, J. Shaffer, Y. An, Q. Liu, B. Wei, H. Jiang, Silicon thin films as anodes for high-performance lithium-ion batteries with effective stress relaxation, Adv. Energy Mater. 2 (2011) 68–73, https://doi.org/10.1002/aenm.201100634.

[26] Y. Zeng, Y. Huang, N. Liu, X. Wang, Y. Zhang, Y. Guo, H.-H. Wu, H. Chen, X. Tang, Q. Zhang, N-doped porous carbon nanofibers sheathed pumpkin-like Si/C composites as free-standing anodes for lithium-ion batteries, J. Energy Chem. 54 (2021) 727–735, https://doi.org/10.1016/j.jechem.2020.06.022.

[27] R. Yu, Y. Pan, Y. Jiang, L. Zhou, D. Zhao, G. Van Tendeloo, J. Wu, L. Mai, Regulating lithium transfer pathway to avoid capacity fading of nano Si through sub-nano scale interfused SiO_x/C coating, Adv. Mater. 35 (2023) 2306504, https://doi.org/10.1002/adma.202306504.

[28] F. Chen, J. Han, D. Kong, Y. Yuan, J. Xiao, S. Wu, D.M. Tang, Y. Deng, W. Lv, J. Lu, F. Kang, Q.H. Yang, 1000 Wh L^{-1} lithium-ion batteries enabled by crosslink-shrunk tough carbon encapsulated silicon microparticle anodes, Natl. Sci. Rev. 8 (2021) nwab012, https://doi.org/10.1093/nsr/nwab012.

[29] Y. Lee, T. Lee, J. Hong, J. Sung, N. Kim, Y. Son, J. Ma, S.Y. Kim, J. Cho, Stress relief principle of micron-sized anodes with large volume variation for practical high-energy lithium-ion batteries, Adv. Funct. Mater. 30 (2020) 2004841, https://doi.org/10.1002/adfm.202004841.

[30] J. Wu, Y. Cao, H. Zhao, J. Mao, Z. Guo, The critical role of carbon in marrying silicon and graphite anodes for high-energy lithium-ion batteries, Carbon Energy. 1 (2019) 57–76, https://doi.org/10.1002/cey2.2.

[31] Y. Li, K. Yan, H. Lee, Z. Lu, N. Liu, Y. Cui, Growth of conformal graphene cages on micrometre-sized silicon particles as stable battery anodes, Nat. Energy. 1 (2016) 15029, https://doi.org/10.1038/nenergy.2015.29.

[32] J. Han, D.M. Tang, D. Kong, F. Chen, J. Xiao, Z. Zhao, S. Pan, S. Wu, Q.H. Yang, A thick yet dense silicon anode with enhanced interface stability in lithium storage evidenced by in situ TEM observations, Sci. Bull. 65 (2020) 1563–1569, https://doi.org/10.1016/j.scib.2020.05.018.

[33] M.S. Kang, I. Heo, S. Kim, J. Yang, J. Kim, S. Min, J. Chae, W.C. Yoo, High-areal-capacity of micron-sized silicon anodes in lithium-ion batteries by using wrinkled-multilayered-graphenes, Energy Storage Mater 50 (2022) 234–242, https://doi.org/10.1016/j.ensm.2022.05.025.

[34] X. Zhang, D. Wang, X. Qiu, Y. Ma, D. Kong, K. Mullen, X. Li, L. Zhi, Stable high-capacity and high-rate silicon-based lithium battery anodes upon two-dimensional covalent encapsulation, Nat. Commun. 11 (2020) 3826, https://doi.org/10.1038/s41467-020-17686-4.

[35] L. Gu, J. Han, M. Chen, W. Zhou, X. Wang, M. Xu, H. Lin, H. Liu, H. Chen, J. Chen, Q. Zhang, X. Han, Enabling robust structural and interfacial stability of micron-Si anode toward high-performance liquid and solid-state lithium-ion batteries, Energy Storage Mater 52 (2022) 547–561, https://doi.org/10.1016/j.ensm.2022.08.028.

[36] L. Sun, Y. Liu, L. Wang, Z. Chen, Z. Jin, Stabilizing porous micro-sized silicon anodes via construction of tough composite interface networks for high-energy-density lithium-ion batteries, Nano Res 17 (11) (2024) 9737–9745, https://doi.org/10.1007/s12274-024-6937-2.

[37] W. He, W. Xu, Z. Li, Z. Hu, J. Yang, G. Qin, W. Teng, T. Zhang, W. Zhang, Z. Sun, X. Yu, Structural design and challenges of micron-scale silicon-based lithium-ion batteries, Adv. Sci. 12 (6) (2025) e2407540, https://doi.org/10.1002/advs.202407540.

[38] W. Xu, Z. Sun, C. Tang, Z. Cheng, W. Sun, A. Du, Q. Zhang, M. Wu, H. Zhang, Biomimetics-driven design of micron-sized SiO composites for high-performance lithium-ion batteries, Adv. Funct. Mater. (2025) 2422743, https://doi.org/10.1002/adfm.202422743.

[39] M. Sun, W. Guo, J. Wang, Q. Zhang, Microenvironment reconstitution-induced collaborative oxyanions-vacancies engineering for enhanced high-mass-loading energy storage, Adv. Funct. Mater. 34 (2024) 2405116, https://doi.org/10.1002/adfm.202405116.

[40] R. Kang, D. Zhang, H. Wang, B. Zhang, X. Zhang, G. Chen, Y. Du, J. Zhang, Synergistic optimization of electronic and lattice structures through Ti-intercalation and Se-vacancy engineering for high-performance aluminum storage, Energy Environ. Sci. 17 (2024) 7135–7146, https://doi.org/10.1039/d4ee02227k.

[41] T. Liu, T. Dong, M. Wang, X. Du, Y. Sun, G. Xu, H. Zhang, S. Dong, G. Cui, Recycled micro-sized silicon anode for high-voltage lithium-ion batteries, Nat. Sustain.. 7 (2024) 1057–1066, https://doi.org/10.1038/s41893-024-01393-9.

[42] S.H. Bhimineni, S.T. Ko, C. Cornwell, Y. Xia, S.H. Tolbert, J. Luo, P. Sautet, First principles study of aluminum doped polycrystalline silicon as a potential anode candidate in Li-ion batteries, Adv. Energy Mater. 14 (2024) 2400924, https://doi.org/10.1002/aenm.202400924.

[43] R. Hu, W. Sun, Y. Chen, M. Zeng, M. Zhu, Silicon/graphene based nanocomposite anode: large-scale production and stable high capacity for lithium ion batteries, J. Mater. Chem. A. 2 (2014) 9118–9125, https://doi.org/10.1039/c4ta01013b.
[44] L. Ouyang, L. Guo, W. Cai, J. Ye, R. Hu, J. Liu, L. Yang, M. Zhu, Facile synthesis of Ge@FLG composites by plasma assisted ball milling for lithium ion battery anodes, J. Mater. Chem. A. 2 (2014) 11280–11285, https://doi.org/10.1039/c4ta01267d.
[45] Z. Ma, L. Tao, D. Liu, Z. Li, Y. Zhang, Z. Liu, H. Liu, R. Chen, J. Huo, S. Wang, Ultrafine nano-sulfur particles anchored on in situ exfoliated graphene for lithium–sulfur batteries, J. Mater. Chem. A. 5 (2017) 9412–9417, https://doi.org/10.1039/c7ta01981e.
[46] W. Sun, R. Hu, H. Liu, M. Zeng, L. Yang, H. Wang, M. Zhu, Embedding nano-silicon in graphene nanosheets by plasma assisted milling for high capacity anode materials in lithium ion batteries, J. Power Sources. 268 (2014) 610–618, https://doi.org/10.1016/j.jpowsour.2014.06.039.
[47] L. Ouyang, Z. Cao, H. Wang, R. Hu, M. Zhu, Application of dielectric barrier discharge plasma-assisted milling in energy storage materials – A review, J. Alloys Compd. 691 (2017) 422–435, https://doi.org/10.1016/j.jallcom.2016.08.179.
[48] C. Wu, X.L. Shi, M. Li, Z. Zheng, L. Zhu, K. Huang, W.D. Liu, P. Yuan, L. Cheng, Z. G. Chen, X. Yao, Argon plasma bombardment induces surface-rich Sn vacancy defects to enhance the thermoelectric performance of polycrystalline SnSe, Adv. Funct. Mater. 34 (2024) 2402317, https://doi.org/10.1002/adfm.202402317.
[49] A.D. Refino, E. Adhitama, M.M. Bela, S. Sadhujan, S. Harilal, C. Eldona, H. Bremers, M.Y. Bashouti, A. Sumboja, M.C. Stan, M. Winter, T. Placke, E. Peiner, H.S. Wasisto, Impact of exposing lithium metal to monocrystalline vertical silicon nanowires for lithium-ion microbatteries, Commun. Mater. 4 (1) (2023), https://doi.org/10.1038/s43246-023-00385-0.
[50] J. Li, T. Wang, Y. Wang, Z. Xu, A. Mateen, W. Yan, H. Li, A. Mujear, J. Chen, S. Deng, G. Gao, C. Zheng, Y. Zhu, Z. Di, Y. Mei, Z. Bao, Solid-liquid-solid growth of doped silicon nanowires for high-performance lithium-ion battery anode, Nano Energy 133 (2025) 110455, https://doi.org/10.1016/j.nanoen.2024.110455.
[51] L.C. Loaiza, L. Monconduit, V. Seznec, Si and Ge-based anode materials for Li-, Na-, and K-ion batteries: a perspective from structure to electrochemical mechanism, Small 16 (5) (2020) e1905260, https://doi.org/10.1002/smll.201905260.
[52] S.H. Bhimineni, S.T. Ko, C. Cornwell, Y. Xia, S.H. Tolbert, J. Luo, P. Sautet, First principles study of aluminum doped polycrystalline silicon as a potential anode candidate in Li-ion batteries, Adv. Energy Mater. 14 (34) (2024), https://doi.org/10.1002/aenm.202400924.
[53] J. Zhang, S. Li, F. Xi, X. Wan, Z. Ding, Z. Chen, W. Ma, R. Deng, Si@SiO /Ag composite anodes with high initial coulombic efficiency derive from recyclable silicon cutting waste, Chem. Eng. J. 447 (2022) 137563, https://doi.org/10.1016/j.cej.2022.137563.
[54] P.K. Lee, M.H. Tahmasebi, S. Ran, S.T. Boles, D.Y.W. Yu, Leveraging titanium to enable silicon anodes in lithium-ion batteries, Small 14 (41) (2018) 201802051, https://doi.org/10.1002/smll.201802051.
[55] Y. Zhong, B. Li, S. Li, S. Xu, Z. Pan, Q. Huang, L. Xing, C. Wang, W. Li, Bi nanoparticles anchored in N-doped porous carbon as anode of high energy density lithium ion battery, Nano-micro Lett 10 (2018) 56, https://doi.org/10.1007/s40820-018-0209-1.
[56] M.K. Sadan, E. Song, H. Yu, J. Yun, T. Kim, J.-H. Ahn, K. Cho, H. Ahn, Extended cycling performance of micron-sized bismuth anodes for lithium-ion batteries: self-healing of an alloy-type anode for lithium batteries, J. Mater. Chem. A. 11 (2023) 15466–15474, https://doi.org/10.1039/d3ta00712j.
[57] J. Chen, G. Zhang, J. Xiao, J. Li, Y. Xiao, D. Zhang, H. Gao, X. Guo, G. Wang, H. Liu, A stress self-adaptive bimetallic stellar nanosphere for high-energy sodium-ion batteries, Adv. Funct. Mater 34 (2023) 2307959, https://doi.org/10.1002/adfm.202307959.
[58] S. Zhang, Y. Zhang, Z. Zhang, H. Wang, Y. Cao, B. Zhang, X. Liu, C. Mao, X. Han, H. Gong, Z. Yang, J. Sun, Bi works as a Li reservoir for promoting the fast-charging performance of phosphorus anode for Li-ion batteries, Adv. Energy Mater. 12 (2022) 2103888, https://doi.org/10.1002/aenm.202103888.
[59] H. Li, T. Yamaguchi, S. Matsumoto, H. Hoshikawa, T. Kumagai, N.L. Okamoto, T. Ichitsubo, Circumventing huge volume strain in alloy anodes of lithium batteries, Nat Commun 11 (1) (2020) 1584, https://doi.org/10.1038/s41467-020-15452-0.
[60] G.G. Zheng Li, Shaozheng Hu, Xiong Zou, Guang Wu, Promotion of activation ability of N vacancies to N_2 molecules on sulfur-doped graphitic carbon nitride with outstanding photocatalytic nitrogen fixation ability, Chin. J. Catal. 40 (2019) 1178–1186. S1872-2067(19)63364-4.
[61] Z. Li, Z. Zhao, S. Pan, Y. Wang, S. Chi, X. Yi, J. Han, D. Kong, J. Xiao, W. Wei, S. Wu, Q.H. Yang, Covalent coating of micro-sized silicon with dynamically bonded graphene layers toward stably cycled lithium storage, Adv. Energy Mater. 13 (2023) 2300874, https://doi.org/10.1002/aenm.202300874.
[62] M. Kamble, V. Waman, A. Mayabadi, A. Funde, V. Sathe, T. Shripathi, H. Pathan, S. Jadkar, Synthesis of cubic nanocrystalline silicon carbide (3C-SiC) films by HW-CVD method, Silicon 9 (2016) 421–429, https://doi.org/10.1007/s12633-015-9358-8.
[63] Y. Huang, B. Shao, Y. Wang, F. Han, Solid-state silicon anode with extremely high initial coulombic efficiency, Energy Environ. Sci. 16 (4) (2023) 1569–1580, https://doi.org/10.1039/d2ee04057c.
[64] W. Huang, Y. Wang, L. Lv, G. Zhu, Q. Qu, H. Zheng, Solid interfacial conversion based on fluorine-silicon reaction enables long-term cycling of full cells with silicon anode, Energy Storage Mater 60 (2023) 102837, https://doi.org/10.1016/j.ensm.2023.102837.
[65] J. Qiu, S. Li, X. Su, Y. Wang, L. Xu, S. Yuan, H. Li, S. Zhang, Bismuth nano-spheres encapsulated in porous carbon network for robust and fast sodium storage, Chem. Eng. J. 320 (2017) 300–307, https://doi.org/10.1016/j.cej.2017.03.054.
[66] X. Shen, Z. Tian, R. Fan, L. Shao, D. Zhang, G. Cao, L. Kou, Y. Bai, Research progress on silicon/carbon composite anode materials for lithium-ion battery, J. Energy Chem. 27 (2018) 1067–1090, https://doi.org/10.1016/j.jechem.2017.12.012.
[67] X. Fu, M. Yang, M. Zhai, C. Zhang, H. Niu, Y. Li, Precision anode vacancy engineering for long-lasting and fast-charging Na-ion batteries, Energy Storage Mater 70 (2024) 103450, https://doi.org/10.1016/j.ensm.2024.103450.
[68] K. Gong, C. Huang, X. Xu, Y. Yao, D. Chen, Y. Tong, P. Lei, Resilient Si@C architecture fabricated by mechanochemical conjugation and thermal reduction for lithium storage: simulation on interfacial state evolution, Chem. Eng. J. 490 (2024) 151632, https://doi.org/10.1016/j.cej.2024.151632.
[69] J. Zhao, J. Chen, M. Zhou, Q. Zhang, X. Li, J. Pan, Ultra-firm phthalocyanine-based tetragonal covalent organic framework layer@nano silicon anode for high durability Li-ion battery, Chem. Eng. J. 488 (2024) 151110, https://doi.org/10.1016/j.cej.2024.151110.
[70] Y. Gao, L. Fan, R. Zhou, X. Du, Z. Jiao, B. Zhang, High-performance silicon-rich microparticle anodes for lithium-ion batteries enabled by internal stress mitigation, Nano-Micro Lett 15 (2023) 222, https://doi.org/10.1007/s40820-023-01190-7.
[71] Y. Wang, J. Song, H. Fan, Y. Luo, Z. Song, Y. Jin, S. Kim, W. Liu, Gradient design for Si-based microspheres as ultra-stable Li-storage anode, Energy Storage Mater 74 (2025) 103939, https://doi.org/10.1016/j.ensm.2024.103939.
[72] Y. Yu, C. Yang, Y. Jiang, J. Zhu, J. Zhang, M. Jiang, Consecutive covalent bonds reconstruct robust dual-interfaces by carbonized binder to enable conductive-additive-free durable silicon anode, Nano Energy 130 (2024) 110108, https://doi.org/10.1016/j.nanoen.2024.110108.
[73] P. Zhou, P. Xiao, L. Pang, Z. Jiang, M. Hao, Y. Li, F. Wu, High-performance yolk-shell structured silicon-carbon composite anode preparation via one-step gas-phase deposition and etching technique, Adv. Funct. Mater. (2024) 2406579, https://doi.org/10.1002/adfm.202406579.
[74] S. Wu, H. Wu, X. Kong, Y. Li, G. Xu, J. Su, J. Huang, G. Wang, X. Ou, *In-situ* construction of dual-coated silicon/carbon composite anode for fast-charging Li-ion batteries, Chem. Eng. J. 502 (2024) 158032, https://doi.org/10.1016/j.cej.2024.158032.
[75] W. Li, J.H. Wang, Y. Li, H. Hsueh, X. Liu, Y. Zhao, S. Huang, X. Li, H.M. Cheng, X. Duan, H.S. Park, Element screening of high-entropy silicon anodes for superior Li-storage performance of Li-ion batteries, J. Am. Chem. Soc. 146 (2024) 21320–21334, https://doi.org/10.1021/jacs.4c01711.
[76] D. Yang, T. Lv, J. Song, J. Chen, L. Hao, Q. Tian, L. Cui, Enabling stable high lithium storage of Si anode via synergistic effects of nanosized Fe_3C and partially graphitized porous carbon, Chem. Eng. J. 496 (2024) 153844, https://doi.org/10.1016/j.cej.2024.153844.
[77] J. Li, M. Wu, Q. Du, G. Zhai, H. He, Simple and safe synthesis of yolk-shell-structured silicon/carbon composites with enhanced electrochemical properties, Molecules 29 (6) (2024), https://doi.org/10.3390/molecules29061301.
[78] D. Han, S. Xiang, J. Cunha, Y. Xie, M. Zhou, Z. Hou, H. Yin, Pre-lithiated silicon/carbon nanosphere anode with enhanced cycling ability and coulombic efficiency for lithium-ion batteries, J. Energy Storage 79 (2024) 110183, https://doi.org/10.1016/j.est.2023.110183.
[79] F.H. Hamid, J. Karunawan, Y. Irmawati, B.T. Laksono, E. Peiner, H.S. Wasisto, F. Iskandar, A. Sumboja, Cationic surfactant assisted electrostatic self-assembly of nitrogen-rich carbon enwrapped silicon anode: unlocking high lithium storage performance, Electrochim. Acta 471 (2023) 143384, https://doi.org/10.1016/j.electacta.2023.143384.
[80] A.M. Firdaus, N.H. Hawari, C.G. Adios, P.M. Nasution, E. Peiner, H.S. Wasisto, A. Sumboja, Unlocking high-current performance in silicon anode: synergistic phosphorus doping and nitrogen-doped carbon encapsulation to enhance lithium diffusivity, Chem. Asian J. 19 (7) (2024) e202400036, https://doi.org/10.1002/asia.202400036.
[81] B. Liu, H. Li, W. Luo, X. Zhang, Z. Liu, P. Yin, R. Zhang, Flexible-rigid covalent nano-template of micron porous silicon towards ultra-robust Li-ion batteries, J. Mater. Chem. A. 12 (17) (2024) 10412–10421, https://doi.org/10.1039/d3ta07447a.
[82] X. Zheng, J. Sun, H. Xia, W. Luo, J. Huang, X. Zhang, H. An, Z. Liu, Formicarium-like micron porous Si synergistically adjusted by surface hard–Soft nanoencapsulation as long-life lithium-ion battery anode, ACS Appl Mater Interfaces 16 (47) (2024) 64774–64783, https://doi.org/10.1021/acsami.4c14210.
[83] Y. Zhang, W. Yang, X. Liu, G. Ma, G. Hu, Z. Liu, R. Yu, D. Zhuang, J. Xu, D. Zhao, L. Mai, L. Zhou, Necklace-structured silicon suboxide-based anode materials with multiple carbon networks for stable lithium storage, Adv. Fun. Mater. 34 (2024) 2315680, https://doi.org/10.1002/adfm.202315680.
[84] B. Peng, Y. Chen, F. Wang, Z. Sun, L. Zhao, X. Zhang, W. Wang, G. Zhang, Unusual site-selective doping in layered cathode strengthens electrostatic cohesion of alkali-metal layer for practicable sodium-ion full cell, Adv. Mater. 34 (2022) e2103210, https://doi.org/10.1002/adma.202103210.
[85] H. Jin, H. Wang, Z. Qi, D.S. Bin, T. Zhang, Y. Wan, J. Chen, C. Chuang, Y.R. Lu, T. S. Chan, H. Ju, A.M. Cao, W. Yan, X. Wu, H. Ji, L.J. Wan, A black phosphorus–Graphite composite anode for Li-/Na-/K-ion batteries, Angew. Chem. Int. Ed. 59 (2019) 2318–2322, https://doi.org/10.1002/anie.201913129.
[86] H. Yu, Y. Cao, L. Chen, Y. Hu, X. Duan, S. Dai, C. Li, H. Jiang, Surface enrichment and diffusion enabling gradient-doping and coating of Ni-rich cathode toward Li-ion batteries, Nat. Commun. 12 (2021) 4564, https://doi.org/10.1038/s41467-021-24893-0.
[87] S. Zhang, F. Ling, L. Wang, R. Xu, M. Ma, X. Cheng, R. Bai, Y. Shao, H. Huang, D. Li, Y. Jiang, X. Rui, J. Bai, Y. Yao, Y. Yu, An open-ended Ni_3S_2-Co_9S_8 heterostructures nanocage anode with enhanced reaction kinetics for superior potassium-ion

batteries, Adv. Mater 34 (2022) e2201420, https://doi.org/10.1002/adma.202201420.